Interface initiation and propagation in liquid demixing with electric fields

Jennifer Galanis and Yoav Tsori
Department of Chemical Engineering, Ben-Gurion University of the Negev, Beer-Sheva, 84105, Israel

We investigate the dynamics of liquid-liquid phase separation confined in a charged concentric cylindrical geometry. Two main time scales characterize the non-equilibrium interface behavior: (1) the lag time t_L for forming an interface, and (2) the relaxation time to equilibrium. We find that t_L increases as parameters (temperature, bulk composition, and surface charge) approach the electrostatic spinodal line in the phase diagram. Close to this line, t_L is proportional to a renormalized bulk concentration with an exponent of -1.16 ± 0.03. The relaxation of the interface to equilibrium can be divided into three phases: early, intermediate (power-law), and late (exponential). During power-law relaxation, the location of the rescaled interface is proportional to time with an exponent of -0.94 ± 0.04. Exponential relaxation occurs as a consequence of finite-size effects, and the associated time constant decreases with decreasing system size (with a power-law scaling), decreasing concentration, and increasing surface charge. The time constant also decreases with increasing (decreasing) temperature when the concentration is below (above) the critical concentration. © *2014 AIP Publishing LLC*. [http://dx.doi.org/10.1063/1.4902406]

I. INTRODUCTION

Research on how electric fields affect phase transitions was motivated in recent decades by an interest in fundamental science, as well as by the potential for technological uses.[1–8] In non-conductive, non-polar liquids, however, spatially uniform electric fields minimally alter the mixing-demixing temperature. A uniform electric field E produces such small changes because the electrostatic energy stored per unit of molecular volume v of a liquid with dielectric constant ε is $\sim v\varepsilon E^2$. For fields smaller than the dielectric breakdown threshold, this energy is much smaller than the thermal energy kT, where k is the Boltzmann's constant and T is the temperature.

Recently, the application of spatially non-uniform electric fields to fluid mixtures has shown great promise.[4] The spatial gradients created by these fields induce large changes to the phase diagram in comparison to uniform electric fields; moreover, new behaviors have been uncovered, such as location-dependent interface properties and unusual kinetic regimes.[9–12] And as non-uniform fields always occur on small scales and are actively used in many devices,[13–15] the potential for further technological development is immense.

While our understanding of liquid demixing with non-uniform electric fields has grown, many open questions still exist. For example, even though the kinetic behavior of the non-equilibrium interface has been outlined,[12] the actual timing of the process remains unknown. For regular (no-field) phase separation, the relaxation to equilibrium depends on the material properties and forces considered. When diffusion is the only method of material transport, the average domain size of the demixed material grows with time to the 1/3 power ($t^{1/3}$).[16] In contrast, the inclusion of hydrodynamics produces a richer domain growth process. The average domain size increases in three different stages (all power-laws with different exponents) when the liquid composition is close to the critical composition,[17–19] but increases via a collision mechanism when the composition is close to the coexistence curve.[17,20]

The inclusion of an electric field is expected to alter these growth mechanisms. Here, we use diffusion-driven kinetics with an electric field in a simple concentric cylinder geometry. Unlike the regular (no-field) cases, we find a delay time in the initiation of an interface that scales with a certain normalization of the mixture composition. Once the demixing process begins, we find that domain growth occurs in multiple stages: early-time, power-law, and exponential. The power-law regime progresses as a -0.94 exponent, rather than the 1/3 exponent typical to no-field condition. We also show that the late-stage exponential growth found in previous investigations[9] is a consequence of finite-size effects.

II. THEORY

We consider the total free energy $\mathcal{F}$ for two liquids (A and B) in a volume V as the sum of mixing $\mathcal{F}_{\mathrm{m}}$, electrostatic $\mathcal{F}_{\mathrm{e}}$, and interfacial $\mathcal{F}_{\mathrm{i}}$ free energies

$$\mathcal{F} = \int_V (\mathcal{F}_{\mathrm{m}} + \mathcal{F}_{\mathrm{e}} + \mathcal{F}_{\mathrm{i}})\mathrm{d}V. \qquad (1)$$

The free energy of mixing is $\mathcal{F}_{\mathrm{m}} = kT f_{\mathrm{m}}/v$. The dimensionless energy density f_{m} has a "double well" shape, and here we use the following Landau expansion of a regular mixing energy around the critical volume fraction ϕ_c:

$$f_{\mathrm{m}} \approx (2 - \chi)(\phi - \phi_c)^2 + \frac{4}{3}(\phi - \phi_c)^4 + const., \qquad (2)$$

where ϕ is the volume fraction of component A, and $\chi \sim 1/T$ is the Flory interaction parameter.[21] We set $\phi_c = 0.5$ and $\chi = 2T_c/T$, where T_c is the critical temperature.

The electrostatic free energy $\mathcal{F}_{\mathrm{e}} = kT f_{\mathrm{e}}/v$ is given by

$$\mathcal{F}_{\mathrm{e}} = -\frac{1}{2}\varepsilon_0 \varepsilon(\phi)|\nabla\psi|^2, \qquad (3)$$

141, 214506-1

where ε_0 is the vacuum permittivity, and ψ is the electrostatic potential ($\mathbf{E} = -\nabla\psi$). The negative sign in Eq. (3) refers to constant potential boundary conditions; the sign should be reversed if the surface charge on the bounding electrodes is prescribed. The constitutive relation $\varepsilon(\phi)$ defines a nontrivial dependence of permittivity on composition, but to understand the basic behavior, we use a linear relation, $\varepsilon(\phi) = (\varepsilon_A - \varepsilon_B)\phi + \varepsilon_B$, where ε_A and ε_B are the dielectric constants for pure liquids A and B, respectively. We set $\varepsilon_A = 5$ and $\varepsilon_B = 3$.

The interfacial free energy $\mathcal{F}_i = kT f_i/v$ includes the energetic penalty associated with composition gradients and is given by[21]

$$f_i = \frac{1}{2}\chi\lambda^2|\nabla\phi|^2, \tag{4}$$

where λ is a constant related to interface width.

The fields ψ and ϕ obey the following Euler-Lagrange equations:

$$\frac{\delta\mathcal{F}}{\delta\psi} = \nabla\cdot[\varepsilon_0\varepsilon(\phi)\nabla\psi] = 0, \tag{5}$$

$$\frac{\delta\mathcal{F}}{\delta\phi} = \mathcal{F}'_m - \frac{1}{2}\varepsilon_0\varepsilon'(\phi)|\nabla\psi|^2 - \nabla\cdot\left[\frac{kT}{v}\chi\lambda^2\nabla\phi\right] - \tilde{\mu} = 0, \tag{6}$$

where the "prime" represents a derivative with respect to ϕ, $\tilde{\mu} = kT\mu/v$ is the scaled chemical potential, and $\nabla(\delta\mathcal{F}/\delta\phi)\cdot\mathbf{n} = 0$ is the boundary condition for Eq. (6), where $\mathbf{n}$ is the unit vector normal to the wall. For closed systems (canonical), μ is adjusted to satisfy the mass conservation constraint, $\langle\phi\rangle = \phi_0$, where ϕ_0 is the average composition. For open systems (grand canonical), μ is set by the large reservoir with composition ϕ_0.

To study the dynamics of liquid demixing, we use the "model H" theoretical framework[22,23] supplemented by Laplace's law to obtain

$$\frac{\partial\phi}{\partial t} + \mathbf{v}\cdot\nabla\phi = D\nabla^2\frac{\delta\mathcal{F}}{\delta\phi}, \tag{7}$$

$$\nabla\cdot(\rho\mathbf{v}) = 0, \tag{8}$$

$$\rho\left[\frac{\partial\mathbf{v}}{\partial t} + (\mathbf{v}\cdot\nabla)\mathbf{v}\right] = \eta\nabla^2\mathbf{v} - \nabla P - \phi\nabla\frac{\delta\mathcal{F}}{\delta\phi}, \tag{9}$$

$$\nabla\cdot[\varepsilon_0\varepsilon(\phi)\nabla\psi] = 0, \tag{10}$$

where $\mathbf{v}$ is the fluid hydrodynamic velocity field, D is the diffusivity constant, P is the pressure, ρ is the fluid density, and η is fluid viscosity. The Cahn-Hilliard equation, Eq. (7), is the continuity equation for the mixture composition.[24] Equation (8) is the continuity equation for the fluid, and Eq. (9) is the Navier-Stokes equation.

We focus on a cylindrical geometry where $\mathcal{F}$ depends only on the radial coordinate. In this geometry, symmetry dictates that $\mathbf{v} = 0$ and hence the problem is reduced to solving Eq. (7) ("model B" dynamics), and Eq. (10). The inner and outer boundaries for the cylindrical geometry are radii R_1 and R_2, respectively, Fig. 1(a). And, the radially symmetric profiles are one-dimensional $\phi = \phi(r)$ and $\psi = \psi(r)$, where r is the distance from the inner cylinder's center. With a constant
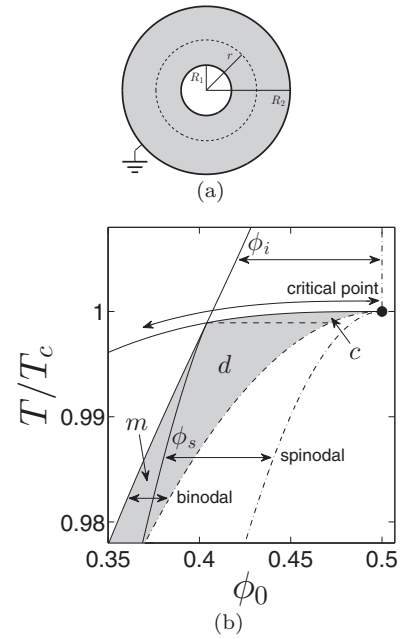

FIG. 1. Model system and stability diagram. (a) Cross section through the diameter of concentric cylinders. Distance r is measured from the center of the cylinder, and the boundaries are located at R_1 and R_2. Shading shows the space occupied by the liquid mixture. (b) Mixing-demixing phase diagram in the $\phi_0 - T$ plane. Arrows link mathematically analogous structures between no-field (dashed-dotted lines) and non-uniform electric field (solid lines) conditions. Shading shows the demixed region for $M \approx 0.017$. The emergence line (dashed line) divides the continuous (c) and discontinuous (d) interface kinetic regimes. m marks the metastable region.

charge density σ on R_1, we obtain $\mathbf{E}(r) = \sigma R_1/(\varepsilon_0\varepsilon(\phi)r)\hat{\mathbf{r}}$. Combining this result with $\mathbf{E} = -\nabla\psi$ in Eq. (6), we get

$$\frac{\delta f}{\delta\phi} = f'_m - \chi M\left(\frac{R_1}{r}\right)^2\frac{\varepsilon'(\phi)}{\varepsilon(\phi)^2} - \nabla\cdot[\chi\lambda^2\nabla\phi] - \mu, \tag{11}$$

where $M = \sigma^2 v/(4kT_c\varepsilon_0)$ is the dimensionless field squared.

III. THE INTERFACE IN TIME

When an electric field is applied to a homogeneous liquid mixture in an open system, events typically first occur near the surface of the electrode and progress outward. Specifically, the material with the larger ε accumulates near the inner electrode, resulting in an increase of the value of $\phi(r)$ at small distances r. If the parameters (ϕ_0, T, M) are within the discontinuous interface formation region of the kinetic phase diagram, Fig. 1(b), the interface first appears on the surface of the electrode, Fig. 2(a). While for continuous interface formation kinetics, Fig. 1(b), the interface first emerges away from the electrode at some distance greater than R_1, Fig. 2(b).

Previous work[12] demonstrated that the behavior of the interface in time through real space can be mapped as a "movement" in parameter space through the equilibrium phase diagram. Here, we investigate in detail the timing of these events and begin by tracking the interface. The location r_i of the dynamic interface corresponds to a rapid change in $\phi(r_i)$ and a double-well structure at $f(r_i)$.[12] The latter criteria distinguishes interfaces from steep concentration gradients and relies on a simplified form of f, which utilizes
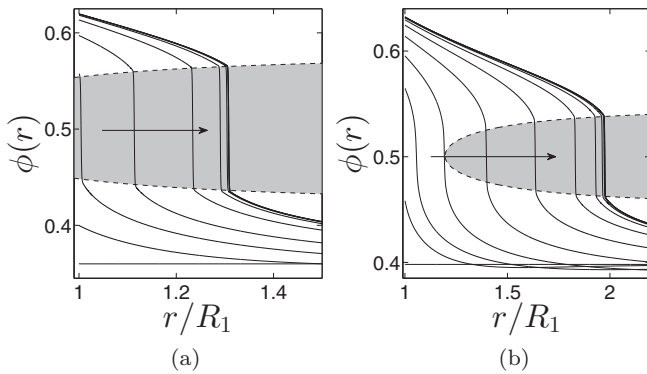
FIG. 2. Relaxation of the concentration profile $\phi(r)$ versus r for (a) discontinuous ($\phi_0 = 0.36$, $T/T_c = 0.992$, $M = 0.069$) and (b) continuous ($\phi_0 \approx 0.4$, $T/T_c = 0.997$, $M = 0.069$) interface transition regimes. Each curve is a different snapshot in time taken at regular intervals on a logarithmic scale. Arrows indicate the direction of movement. Gray shows regions where an interface can exist.

$f_i \to 0$. Usually, rapid changes in ϕ (largest values of $|\partial\phi/\partial r|$) roughly correspond to where $\phi(r_i) \approx 0.5$, and for simplicity we assume $\phi(r_i) = 0.5$.

Typical graphs of r_i versus time t for a constant T and M with various values of ϕ_0 are shown for discontinuous, Fig. 3(a), and continuous, Fig. 4(a), interface formation kinetics. The moment where the electric field is applied is defined as $t = 0$, and solid lines track interface movement. For the contin-
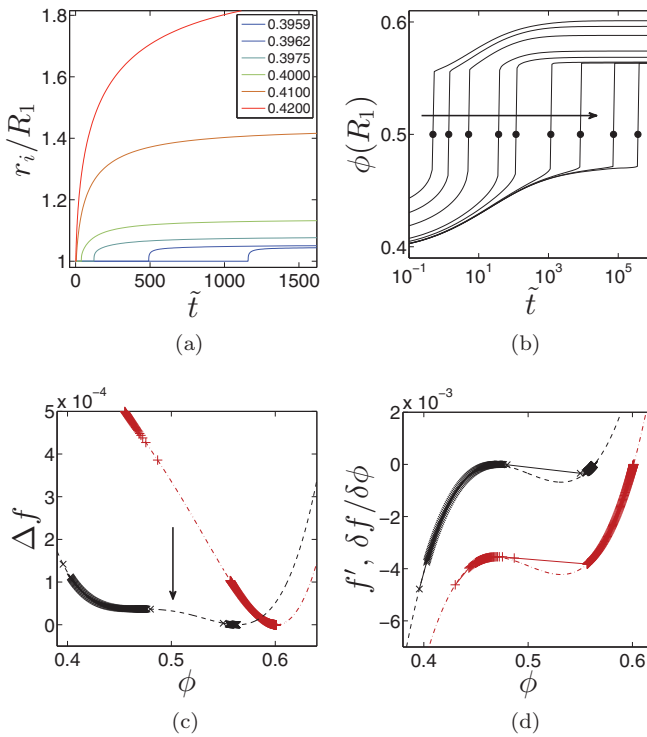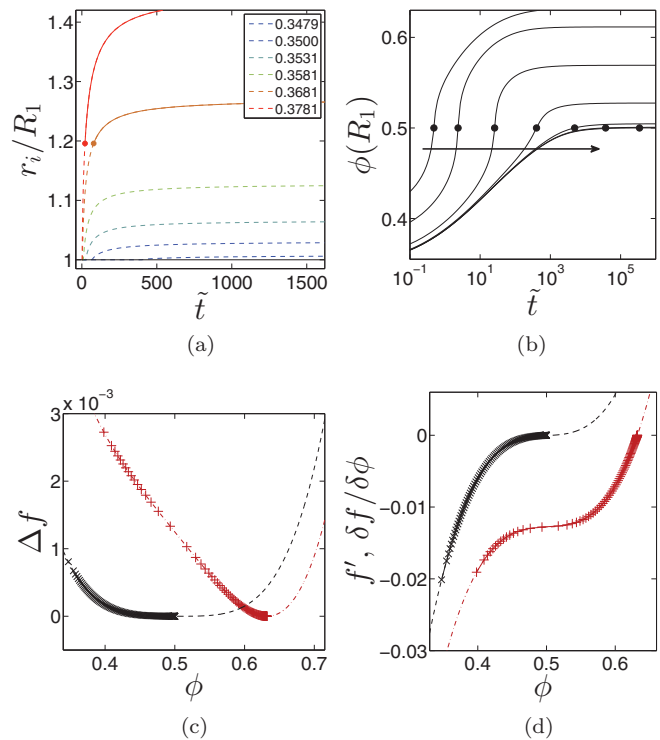

FIG. 4. Tracking the interface r_i in the continuous interface formation kinetic regime. (a) Location of the interface r_i versus normalized time $\tilde{t}$ for various values of ϕ_0, where $\phi_0 \to \phi_i$ (see Fig. 1(b)). Symbols in (a) mark the appearance of the interface, while solid lines track the movement of an interface. Dashed lines track the movement of the steepest concentration gradient ("largest" values of $|\partial\phi/\partial r|$, but no true interface). (b) Behavior of $\phi(r)$ at $r = R_1$ versus time $\tilde{t}$ for $\phi_0 \approx 0.398$ to ≈ 0.363 (arrow). Symbols in (c) and (d) mark the time $\tilde{t}_L$ for the initiation of a gradient. (c) and (d) Δf and f' (or $\delta f/\delta\phi$) at $r = R_1$ versus ϕ for $\phi_0 = 0.3981$ (red) and 0.3473 (black). In all figures, $T/T_c = 0.997$ and $M \approx 0.069$.

uous interface formation kinetics, Fig. 4(a), we also monitor the movement of the steepest concentration gradient (largest values of $|\partial\phi/\partial r|$ for all r, dashed lines) before a true interface emerges (symbols).

By focusing on the discontinuous interface kinetics, Fig. 3(a), two general events appear to characterize liquid behavior in time: (1) the lag time before an interface emerges, and (2) the relaxation of the interface to equilibrium (long-time steady-state). These two behaviors can also occur in continuous interface kinetics when steep concentration gradients, in addition to interfaces, are included in the analysis.

IV. INTERFACE LAG TIME

For discontinuous interface formation kinetics, the time t for an interface to emerge increases as ϕ_0 decreases, red to blue in Fig. 3(a). To better visualize this effect, we use the fact that the interface begins at R_1 and show the behavior of $\phi(R_1)$ versus a dimensionless time $\tilde{t} = DkTt/R_1^2 v$, Fig. 3(b). The time $\tilde{t}_L$ when $\phi(R_1) = 0.5$ (Fig. 3(b), symbols) marks the time when the interface first emerges, or the lag time. The divergent increase in $\tilde{t}_L$ for decreasing ϕ_0 is shown in Fig. 5(a).

The limiting concentration for the increase in $\tilde{t}_L$ is the concentration $\phi_s(T, M)$, dashed line in Fig. 5(a), associated with the electrostatic spinodal line, Fig. 1(b). This line
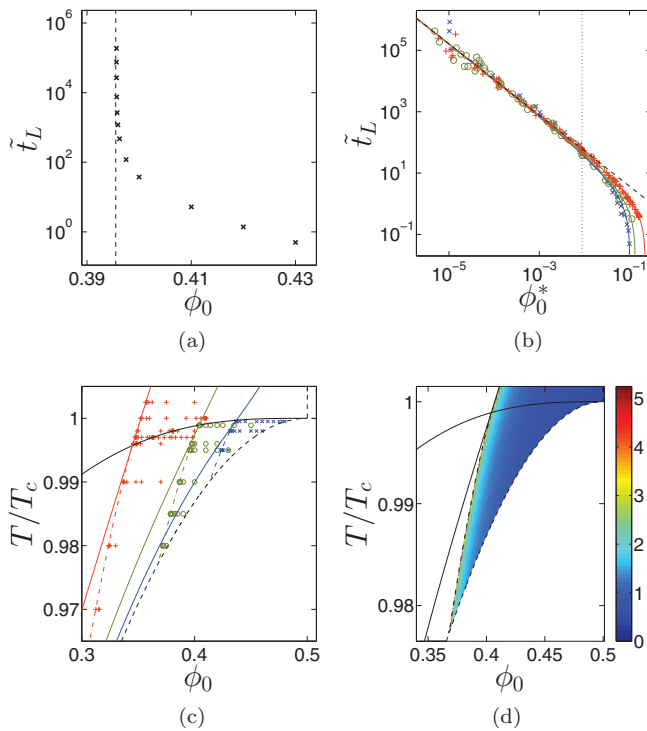

FIG. 3. Tracking the interface r_i in the discontinuous interface formation kinetic regime. (a) Location of the interface r_i versus normalized time $\tilde{t}$ for various values of ϕ_0, where $\phi_0 \to \phi_s$ (see Fig. 1(b)). (b) Behavior of $\phi(r)$ at $r = R_1$ versus time $\tilde{t}$ for $\phi_0 = 0.43$ to ≈ 0.3956 (arrow). Symbols mark the dimensionless lag time $\tilde{t}_L$ for the formation of the interface. (c) and (d) $\Delta f = f(\phi, r) - f_{\min}(\phi, r)$ and f' (or $\delta f/\delta\phi$) at $r = R_1$ versus ϕ for $\phi_0 = 0.43$ (red) and 0.3956 (black). Arrow in (c) shows the precursor to an energetic barrier. In all figures, $T/T_c = 0.995$ and $M \approx 0.017$.

FIG. 5. Lag time for the initiation of either an interface or steep concentration gradient (large $|\partial\phi/\partial r|$) at $r = R_1$. (a) Dimensionless lag time $\tilde{t}_L$ versus bulk concentration ϕ_0 for $T/T_c = 0.995$ and $M \approx 0.017$. $\tilde{t}$ diverges as ϕ_0 approaches ϕ_s (dashed vertical line). (b) $\tilde{t}_L$ versus rescaled bulk concentration ϕ_0^* (see text) for various values of ϕ_0, T, and M. Black dashed line shows least squares fit to Eq. (12) of the data to the left of the dotted line. Solid colored lines show the fits to Eq. (13). (c) Symbols show data used in (b) in the $\phi_0 - T$ plane, where $M \approx 0.005$ (blue, ×), 0.017 (green, ○), and 0.069 (red, +). Solid black line shows the electrostatic line of critical points, while dashed line shows the regular (no-field) binodal. Colored solid and dashed-dotted lines mark the electrostatic binodal and electrostatic spinodal, respectively, for each value of M. (d) Using Eq. (13), extrapolation of the behavior of the lag time on the $\phi_0 - T$ plane for $M \approx 0.017$.

separates spontaneous transitions from metastable states in the $\phi_0 - T$ plane, and is characterized by the functional form of $f(\phi, r)$ on the surface ($r = R_1$) of the electrode.[12] Specifically, if f has a "double-well" form as a function of ϕ at $r = R_1$, an energetic barrier exists that prevents spontaneous transitions. In contrast, a single-well f at this distance enables spontaneous transitions.

Therefore, an understanding for the existence of $\tilde{t}_L$ can be found by inspecting the shape of $f(\phi, r = R_1)$ for conditions (ϕ_0, T, M) near the electrostatic spinodal. As ϕ_0 approaches ϕ_s from within the discontinuous interface formation region, the single-well form of $f(R_1)$ gradually approaches a double-well form as the precursor of a barrier enlarges. Figures 3(c) and 3(d) compare f and its derivatives, respectively, for ϕ_0 close to (black, ×) and far away from (red, +) ϕ_s. The arrow marks the precursor to a barrier.

The description thus far contains arguments reminiscent to the kinetics of relaxation near the regular (no-field) spinodal line. But unlike the no-field counterpart, a lag time also appears to occur with the initial formation of steep concentration gradients, Fig. 4(a), even in the regions of the $\phi_0 - T$ plane where no true demixing occurs (non-shaded areas in Fig. 1(b)). Figure 4(b) shows $\phi(R_1)$ versus $\tilde{t}$ for the data in

Fig. 4(a). Above the emergence line, Fig. 1(a), the lag time $\tilde{t}_L$ to form a steep concentration gradient on the electrode surface increases (Fig. 4(b), symbols) when ϕ_0 approaches the limiting concentration ϕ_i, as defined in Fig. 1(b). Figures 4(c) and 4(d) compare f and its derivatives, respectively, for ϕ_0 close to (black, ×) and far away from (red, +) ϕ_i. As no double well exists in f at $r = R_1$, the increase in $\tilde{t}_L$ results instead from a widening of the single-well basin of $f(\phi, r = R_1)$. As this widening in f is in part due to $T \approx T_c$, we expect $\tilde{t}_L$ to vanish when $T \gg T_c$.

Figure 1(b) details the relation of mathematically analogous structures between the non-uniform electric field and no-field phase diagrams.[11,12] Given these analogies, we borrow ideas from critical behavior[25] and plot $\tilde{t}_L$ versus a rescaled concentration ϕ_0^*, where $\phi_0^* = (\phi_0 - \phi_s)/\phi_s$ below and $\phi_0^* = (\phi_0 - \phi_i)/\phi_i$ above the emergence line, Fig. 1(b). Figure 5(b) shows how the lag time from a wide range of data in the $\phi_0 - T$ plane, Fig. 5(c), collapses when rescaled with ϕ_0^*. Interestingly, the data with or without a true interface, Fig. 5(c), behave indistinguishably, Fig. 5(b).

For a region of ϕ_0^* that spans many decades on a log-log plot, t_L is linear, Fig. 5(b). Performing a least squares fit of the data to a power-law function, we find

$$t_L = A\left(\phi_0^*\right)^{\alpha}, \quad (12)$$

where $\alpha = -1.16 \pm 0.03$ and the constant $A = 0.56 \pm 0.07$. Typically, a simple power-law like Eq. (12) cannot fit an entire dataset, especially when parameters are far from a critical point.[25] Since analogous nonlinearity is observed in Fig. 5(b) for larger ϕ_0^*, we used an upper-bound cutoff of $\phi_0^* \approx 0.009$ (right vertical dotted line) when performing the fit.

While the linear behavior occurs for "small" values of ϕ_0^*, the general collapse of the data (especially for a particular value of M) continues further. We remove the upper-bound cutoff in the data and include a correction term[25] so that Eq. (12) becomes

$$t_L = A\left(\phi_0^*\right)^{\alpha}\left[1 + B\left(\phi_0^*\right)^{\beta}\right], \quad (13)$$

where $\beta = 0.44 \pm 0.16$, $B = -2.7 \pm 1$ for $M \approx 0.005$, $\beta = 0.46 \pm 0.11$, $B = -2.5 \pm 0.7$ for $M \approx 0.017$, and $\beta = 0.58 \pm 0.08$, $B = -2.4 \pm 0.4$ for $M \approx 0.069$. Using Eq. (13), we show the general behavior of t_L in the $\phi_0 - T$ plane for $M \approx 0.017$, Fig. 5(d).

V. INTERFACE RELAXATION: POWER-LAW SCALING

After the interface forms, the relaxation to equilibrium occurs via a complex manner in time. Figure 6(a) shows similar data as Fig. 3(a) plotted as r_i versus a rescaled time, $\tilde{t} - \tilde{t}_L$, and focuses on the early time behavior. Additionally, Fig. 3(b) shows an extended view of the interface behavior in time by using a standard normalization for interface location $\tilde{r}_i$ given by

$$\tilde{r}_i = \frac{r_i(\tilde{t}) - r_i(\tilde{t} \to \infty)}{r_i(\tilde{t} = \tilde{t}_L) - r_i(\tilde{t} \to \infty)}. \quad (14)$$

Despite the complicated dynamics, three general time regimes for interface relaxation become apparent: (1) "early-time" relaxation, (2) power-law relaxation, and (3) exponential
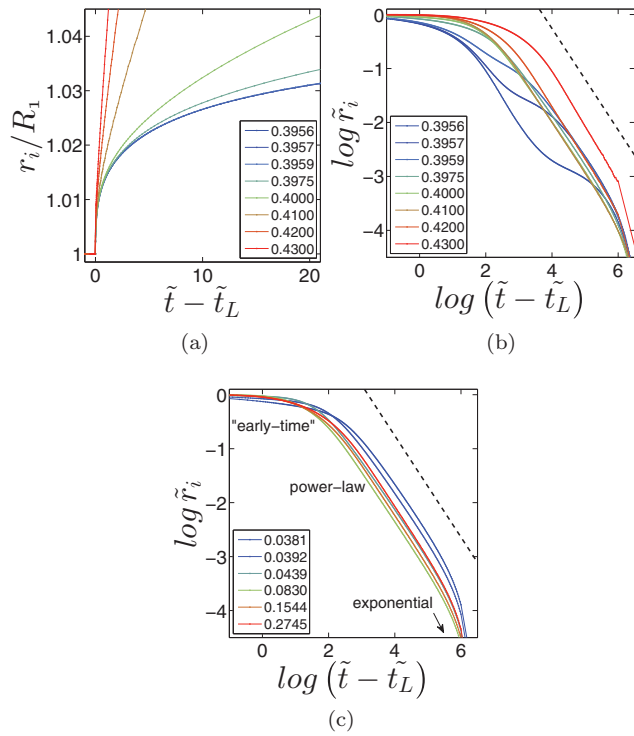
(a)   (b)   (c)

FIG. 6. Movement of the interface r_i with time. (a) Normalized interface location r_i versus time $\tilde{t}$ for $T/T_c = 0.995$, $M \approx 0.017$, and various values of ϕ_0. (b) Same data as (a) with a rescaled interface location $\tilde{r}_i$ from Eq. (14). (c) Rescaled interface location $\tilde{r}_i$ versus time $\tilde{t}$ for $\phi_0 = 0.37$, $T/T_c = 0.995$, and various values of M. Black dashed lines in (b) and (c) show a power-law with an exponent of -0.94.

relaxation. Since the early-time behavior continues for longer time periods for ϕ_0 "close to" ϕ_s (Fig. 6(b)), Fig. 6(c) more clearly shows these regimes with data far enough away from ϕ_s.

After the early-time relaxation, the power-law relaxation follows

$$\tilde{r}_i = C(\tilde{t} - \tilde{t}_L)^\gamma, \qquad (15)$$

where, to a first approximation, interface relaxation behaves independently of the parameters (ϕ_0, T, M), yielding $\gamma = -0.94 \pm 0.04$. For comparison, dashed lines in Figs. 6(b) and 6(c) show power-law behavior with $\gamma = -0.94$. Finally, the third time regime, exponential relaxation, is fully addressed in Sec. VI.

VI. FINITE SIZE EFFECTS: EXPONENTIAL RELAXATION

For liquid-liquid demixing under non-uniform electric fields, the constraint of material conservation in closed systems produces different equilibrium (long-time) concentration profiles $\phi(r)$ in comparison to open systems with the same parameters (ϕ_0, T, M).[10,11] These differences, however, can be explained by considering an alternative "effective bulk" concentration acting on the closed system.[11] In contrast, recent investigations[12] demonstrate that the dynamics of the non-equilibrium interface are equivalent for open and closed systems for the same parameters ($\phi_0 < \phi_c$, T, M) during early times. Therefore, at some "intermediate" time, the presence of a second boundary at R_2 influences the behavior of the inter-
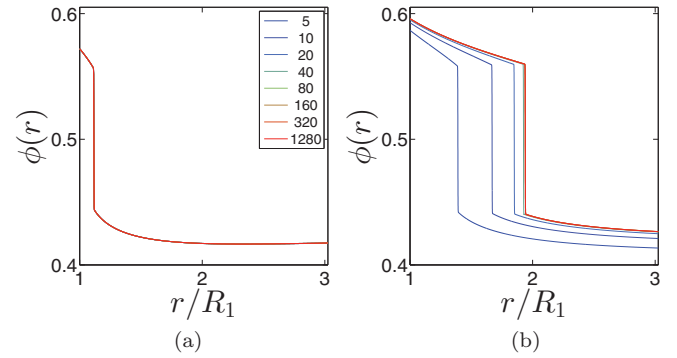

(a)   (b)

FIG. 7. Finite size effects in the $\phi(r)$ profiles with time. $\phi(r)$ versus normalized distance r at $\tilde{t} = 10$ (a) and $10\,000$ (b) for $\phi_0 = 0.42$, $T/T_c = 0.995$, $M \approx 0.017$, and various ratios R_2/R_1.

face in a closed system such that the dynamics diverge from that of an open system.

To investigate these finite-size effects, we compare the time evolution of the liquid under various confinements. Figure 7 shows typical examples of $\phi(r)$ versus r, where the color from red to blue signifies decreasing ratios R_2/R_1 while all other parameters (ϕ_0, T, M) are held constant. Indeed, the $\phi(r)$ profiles between various values of R_2 match during early times, Fig. 7(a), but differ during later times, Fig. 7(b).

To better visualize the relaxation process, we track the location r_i of the interface through time, Fig. 8(a). While initially the interface forms and moves in a manner that is independent of confinement, the interface location systematically diverges from that of open systems at later times. Specifically, as R_2 decreases (color from red to blue), the interface movement slows and eventually stalls at earlier times.

Rather than the standard normalization of distance $\tilde{r}_i$ (Eq. (14)), the systematic and progressive deviation of the closed system r_i from the open system suggests an alternative normalized distance $\tilde{r}_i^*$,

$$\tilde{r}_i^*(\tilde{t}) = \frac{r_i(\tilde{t}) - r_i^*(\tilde{t} \to \infty)}{r_i(\tilde{t} = 0) - r_i^*(\tilde{t} \to \infty)}, \qquad (16)$$

where the *open* system equilibrium interface location $r_i^*(\tilde{t} \to \infty)$ serves as the reference. Analogous methods for determining finite size effects have been used elsewhere.[26]

We approximate $r_i^*(\tilde{t} \to \infty)$ by using data from the largest system size, $R_2/R_1 = 5120$, such that $r_i^*(\infty) = r_i(\tilde{t} \to \infty, R_2 \to \infty) \approx r_i(\tilde{t} \to \infty, R_2 = 5120R_1)$. Results are shown in Fig. 8(b). The red curve in Fig. 8(b) indicates the reference curve, where the three time regimes (introduced in Sec. V) are easily observed. Decreasing values of R_2/R_1 are shown in color from orange progressing to blue.

The normalization $\tilde{r}_i^*$ offers a convenient and standardized way to determine the time $\tilde{t}_d$ when the interface behavior of a closed system diverges from that of an open system. Specifically, we obtain $\Delta\tilde{r}_i^*(R_2) = \tilde{r}_i^*(R_2) - \tilde{r}_i^*(R_2 \to \infty)$ and apply a threshold value cutoff for $\Delta\tilde{r}_i^*(R_2)$ to estimate $\tilde{t}_d$, black symbols in Fig. 8(b). The variation $\tilde{t}_d$ versus R_2/R_1, Fig. 8(d), suggests a power-law relation

$$\tilde{t}_d \propto (R_2/R_1)^\delta, \qquad (17)$$
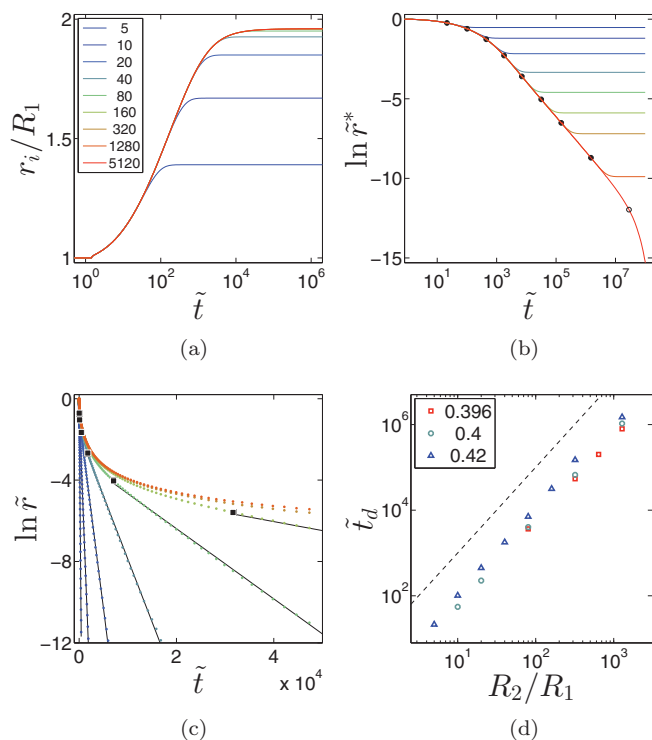
where $\delta = 2 \pm 0.06$.

(a)

(b)

(c)

(d)

FIG. 8.   Finite size effect in interface movement. (a) Location of the interface r_i versus time $\tilde{t}$ for $\phi_0 = 0.42$, $T/T_c = 0.995$, $M \approx 0.017$, and increasing ratios R_2/R_1 (colors blue to red). (b) Same data as (a), plotted as normalized distance $\tilde{r}^*$ (Eq. (16)) versus $\tilde{t}$. Filled symbols mark $\tilde{t}_d$. The open symbol estimates $\tilde{t}_d$ using Eq. (17). (c) Color shows the same data as (a), plotted as normalized distance $\tilde{r}$ (Eq. (14)) versus $\tilde{t}$. Black lines show the fits to Eq. (18) for data $\tilde{t} \geq \tilde{t}_d$ (black symbols). (d) Time $\tilde{t}_d$ versus R_2/R_1 for various values of ϕ_0. Dashed line shows a power-law with an exponent of 2.

The trend of the curves in Fig. 8(b) as a function of R_2 is consistent with the idea that the long-time interface in open systems relaxes as a power law, while finite-sized systems eventually display exponential relaxation.[27–29] The exponential relaxation in the data is more readily viewed in a semi-log plot, Fig. 8(c), of $\tilde{r}_i$ versus $\tilde{t}$. Black lines in Fig. 8(c) show the fit of the data (with a lower bound cutoff of $\tilde{t} \geq \tilde{t}_d$ [black symbols]) to

$$\tilde{r}_i(\tilde{t}) = \exp[-(\tilde{t} - \tilde{t}_L)/\tau], \qquad (18)$$

where τ is the relaxation constant. The values of τ as a function of the ratio R_2/R_1 are shown in Fig. 9(a). And similar to $\tilde{t}_d$, the variation of τ versus R_2/R_1, Fig. 9(a), also suggests a power-law relation

$$\tau \propto (R_2/R_1)^\zeta, \qquad (19)$$

where $\zeta = 1.93 \pm 0.05$. Finally, we show τ as a function of ϕ_0 and M for $R_2/R_1 = 5$ (Figs. 9(b)– 9(d)). In general, τ decreases with decreasing ϕ_0, and increasing M. The variation of τ on T, however, depends on whether or not ϕ_0 is above or below ϕ_c. For $\phi_0 < \phi_c$, τ decreases with increasing T (Figs. 9(b) and 9(c)). In contrast, τ decreases with decreasing T for $\phi_0 > \phi_c$ (Figs. 9(b) and 9(c)).
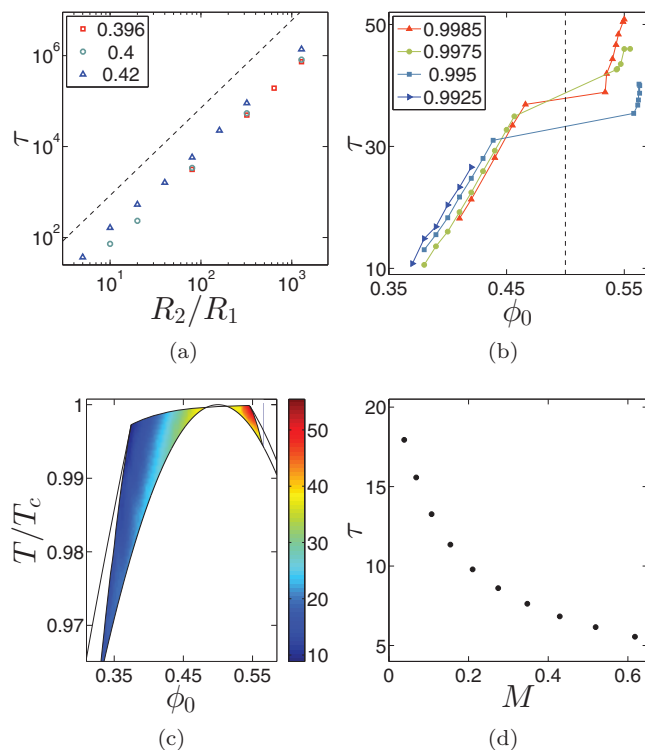

(a)

(b)

(c)

(d)

FIG. 9.   Interface relaxation time τ in finite-sized systems. (a) Relaxation time τ versus R_2/R_1 for various values of ϕ_0. Dashed line shows a power-law with an exponent of 1.925. (b) τ versus ϕ_0 for various values of T/T_c for $M \approx 0.044$, $R_2/R_1 = 5$. Dashed line marks ϕ_c. (c) Color shows τ in the $\phi_0 - T$ plane for $M \approx 0.044$, $R_2/R_1 = 5$. Solid lines mark the boundary of the closed system stability diagram. (d) τ versus M for $\phi_0 = 0.4$, $T/T_c = 0.9957$.

VII. CONCLUSION

Using a simple model system, we find that spatially non-uniform electric fields generate a rich array of dynamic behavior. A lag-time exists before an interface appears between the two liquids. This time delay increases as parameters (temperature, bulk concentration, and surface charge) approach the electrostatic spinodal line, and scales as a simple power-law when considering a renormalized bulk concentration. Once an interface forms, it relaxes to the equilibrium state via three time regimes (early, intermediate, and late). The middle phase is governed by a power-law relaxation, while the late phase is a consequence of finite size effects and follows an exponential decay.

A concise characterization of the early-time behavior still remains an open question. It is clear from the theory that the rate of domain growth during these early times both decreases and increases by a currently unknown mechanism. For no-field liquid-liquid demixing (with hydrodynamics), the crossover of domain growth to different time regimes occurs when different forces compete, for example, surface tension versus gravity during late relaxation times.[17]

Similarly, the dynamic behavior of phase transitions in electric field gradients is dictated by the delicate balance between interfacial forces (scaling as area) and electrostatic forces (scaling as volume). In non-polar liquids, where screening is absent, the electrostatic forces are governed by the specific boundary conditions at remote surfaces, which may produce these rich and fascinating dynamics.

Finally, in this paper we have also focused on radial symmetry, where the solutions are strictly *r*-dependent. It is possible that the removal of this constraint will produce non-radial instabilities that will modify the timing of events.

ACKNOWLEDGMENTS

[1] L. D. Landau and E. M. Lifshitz, *Elektrodinamika Sploshnykh sred* (Nauka, Moscow, 1957).

[2] P. Debye and K. Kleboth, J. Chem. Phys. **42**, 3155 (1965).

[3] A. Onuki, Europhys. Lett. **29**, 611 (1995).

[4] Y. Tsori, F. Tournilhac, and L. Leibler, Nature (London) **430**, 544 (2004).

[5] G. Zhang and G. Qiao, J. Chem. Phys. **139**, 134903 (2013).

[6] H. G. Schoberth, C. W. Pester, M. Ruppe, V. S. Urban, and A. Boeker, ACS Macro Lett. **2**, 469 (2013).

[7] K. Orzechowski, M. Adamczyk, A. Wolny, and Y. Tsori, J. Phys. Chem. B **118**, 7187 (2014).

[8] Y. Tsori, Rev. Mod. Phys. **81**, 1471 (2009).

[9] G. Marcus, S. Samin, and Y. Tsori, J. Chem. Phys. **129**, 061101 (2008).

[10] S. Samin and Y. Tsori, J. Chem. Phys. **131**, 194102 (2009).

[11] J. Galanis and Y. Tsori, Phys. Rev. E **88**, 012304 (2013).

[12] J. Galanis and Y. Tsori, J. Chem. Phys. **140**, 124505 (2014).

[13] K. Khoshmanesh, S. Nahavandi, S. Baratchi, A. Mitchell, and K. Kalantar-zadeh, Biosens. Bioelectron. **26**, 1800 (2011).

[14] R. Pethig, Biomicrofluidics **4**, 022811 (2010).

[15] T. Z. Jubery, S. K. Srivastava, and P. Dutta, Electrophoresis **35**, 691 (2014).

[16] I. M. Lifshitz and V. V. Slyozov, J. Phys. Chem. Solids **19**, 35 (1961).

[17] E. Siggia, Phys. Rev. A **20**, 595 (1979).

[18] Y. Chou and W. Goldburg, Phys. Rev. A **20**, 2105 (1979).

[19] T. Koga and K. Kawasaki, Phys. Rev. A **44**, R817 (1991).

[20] K. Binder and D. Stauffer, Phys. Rev. Lett. **33**, 1006 (1974).

[21] S. Safran, *Statistical Thermodynamics of Surfaces, Interfaces, and Membranes* (Westview Press, New York, 1994).

[22] P. C. Hohenberg and B. I. Halperin, Rev. Mod. Phys. **49**, 435 (1977).

[23] A. Bray, Adv. Phys. **51**, 481 (2002).

[24] J. W. Cahn and J. E. Hilliard, J. Chem. Phys. **28**, 258 (1958).

[25] H. E. Stanley, *Introduction to Phase Transitions and Critical Phenomena* (Clarendon Press, Oxford, 1971).

[26] S. Majumder and S. K. Das, Phys. Rev. E **81**, 050102 (2010).

[27] J. Williams, J. Phys. A **18**, 49 (1985).

[28] N. Ito, Physica A **196**, 591 (1993).

[29] C. Munkel, D. Heermann, J. Adler, M. Gofman, and D. Stauffer, Physica A **193**, 540 (1993).